G11.92−0.61-MM2: A BONAFIDE MASSIVE PRESTELLAR CORE?

C. J. CYGANOWSKI[1,2], C. L. BROGAN[3], T. R. HUNTER[3], D. GRANINGER[2], K. I. ÖBERG[2],
A. VASYUNIN[4,5,6], Q. ZHANG[2], R. FRIESEN[7], AND S. SCHNEE[3]

[1] Scottish Universities Physics Alliance (SUPA), School of Physics and Astronomy, University of St. Andrews,
North Haugh, St Andrews, Fife KY16 9SS, UK; cc243@st-andrews.ac.uk
[2] Harvard-Smithsonian Center for Astrophysics, Cambridge, MA 02138, USA
[3] NRAO, 520 Edgemont Rd, Charlottesville, VA 22903, USA
[4] School of Physics and Astronomy, University of Leeds, Leeds LS2 9JT, UK
[5] Max-Planck-Institut fr Extraterrestrische Physik (MPE), Giessenbachstr.1, D-85748 Garching, Germany
[6] Ural Federal University, Ekaterinburg, Russia
[7] Dunlap Institute for Astronomy and Astrophysics, University of Toronto, 50 St. George Street, Toronto, ON M5S 3H4, Canada

ABSTRACT

Core accretion models of massive star formation require the existence of stable massive starless cores, but robust observational examples of such objects have proven elusive. We report subarcsecond-resolution Submillimeter Array (SMA) 1.3 mm, 1.1 mm, and 0.88 mm and Very Large Array 1.3 cm observations of an excellent massive starless core candidate, G11.92−0.61–MM2, initially identified in the course of studies of GLIMPSE Extended Green Objects (EGOs). Separated by ∼7″.2 from the nearby MM1 protostellar hot core, MM2 is a strong, compact dust continuum source (submillimeter spectral index $\alpha = 2.6 \pm 0.1$), but is devoid of star formation indicators. In contrast to MM1, MM2 has no masers, no centimeter continuum, and no (sub)millimeter wavelength line emission in ∼24 GHz of bandwidth observed with the SMA, including N_2H^+(3–2), HCO^+(3–2), and HCN(3–2). Additionally, there is no evidence for an outflow driven by MM2. The (sub)millimeter spectral energy distribution of MM2 is best fit with a dust temperature of ∼17–19 K and luminosity of ∼5–7 $L_\odot$. The combined physical properties of MM2, as inferred from its dust continuum emission, are extreme: $M \gtrsim 30\, M_\odot$ within a radius <1000 AU, $N_{H_2} > 10^{25}\, cm^{-2}$ and $n_{H_2} > 10^9\, cm^{-3}$. Comparison of the molecular abundance limits derived from our SMA observations with gas-grain chemical models indicates that extremely dense ($n(H) \gg 10^8\, cm^{-3}$), cold (<20 K) conditions are required to explain the lack of observed (sub)millimeter line emission, consistent with the dust continuum results. Our data suggest that G11.92−0.61–MM2 is the best candidate for a bonafide massive prestellar core found to date, and a promising target for future higher-sensitivity observations.

Key words: astrochemistry – ISM: individual objects (G11.92-0.61) – ISM: molecules – stars: formation – stars: protostars – submillimeter: ISM

Online-only material: color figures

1. INTRODUCTION

Do massive starless cores exist in nature? The answer to this question is a key discriminant between the two major classes of models for massive star formation: "core accretion" and "competitive accretion" (recently reviewed by Tan et al. 2014). Core accretion models require, as initial conditions, gravitationally bound, starless massive cores (e.g., McKee & Tan 2002, 2003; Myers et al. 2013); competitive accretion models do not (e.g., Smith et al. 2009; Bonnell & Smith 2011). In the core accretion scenario, forming a high-mass star ($M_{ZAMS} > 8\, M_\odot$) requires an initial core mass ⩾2–3 times larger (Alves et al. 2007; Rathborne et al. 2009; Tan et al. 2014).

Observationally, examples of massive starless cores— <0.1 pc structures likely to form single stars or small multiple systems—have proven elusive. In addition to the candidates disqualified by sensitive mid-infrared surveys with *Spitzer* and *Herschel*, centimeter-submillimeter interferometers have revealed molecular outflows and/or masers—indisputable signs of active star formation—in past "starless" core candidates (e.g., Bontemps et al. 2010, Duarte-Cabral et al. 2013 in Cygnus-X). In this context, the best chances for identifying robust massive starless core candidates lie in massive star-forming regions for which comprehensive, high-resolution multiwavelength data sets are available.

In studying GLIMPSE Extended Green Objects (EGOs; Cyganowski et al. 2008), we have identified an excellent candidate for a massive starless core: G11.92−0.61-MM2. Our initial Submillimeter Array (SMA) 1.3 mm observations of the EGO G11.92−0.61 revealed a massive (proto)cluster, containing three compact cores (Cyganowski et al. 2011b, resolution ∼2″.4). MM2 exhibited strong millimeter continuum emission, but, remarkably, no line emission across ∼4 GHz of SMA bandwidth. MM2 also lacks other star formation indicators: MM2 is not associated with CH_3OH maser or centimeter continuum emission, does not drive a molecular outflow, and has no H_2O maser emission (Cyganowski et al. 2009, 2011a, 2011b; Hofner & Churchwell 1996; Breen & Ellingsen 2011). In this Letter, we present subarcsecond-resolution SMA[8] observations of G11.92−0.61 at 1.3, 1.1, and 0.88 mm, totalling ∼24 GHz of bandwidth. Together with Karl G. Jansky Very Large Array (VLA) 1.3 cm NH_3 and continuum observations, we use these data to constrain the physical and chemical properties of MM2, and find that MM2 is the best candidate for a bonafide massive starless core discovered to date. Throughout, we adopt the maser parallax distance of $3.37^{+0.39}_{-0.32}$ kpc (Sato et al. 2014).

---

[8] The Submillimeter Array is a joint project between the Smithsonian Astrophysical Observatory and the Academia Sinica Institute of Astronomy and Astrophysics and is funded by the Smithsonian Institution and the Academia Sinica.

Table 1
Observing Parameters

Parameter	SMA 1.3 mm	SMA 1.1 mm	SMA 0.88 mm	VLA 1.3 cm
Observing date (UT)	2011 Aug 28	2013 May 31	2011 Aug 19	2010 Aug 25, 2011 Jan 30
Project code	2011A-S076	2013A-S043	2011A-S076	AB1346
Configuration	Very Extended	Extended	Extended	D + CnB
Number of antennas	8	7	8	21, 21
$\tau_{225\,GHz}$	~0.05	~0.1–0.15	~0.04–0.08	n/a
T_{sys} (source transit)	~90 K	~200 K	~200 K	n/a
Phase Center (J2000):				
R.A.	$18^h13^m58\overset{s}{.}10$	$18^h13^m58\overset{s}{.}10$	$18^h13^m58\overset{s}{.}10$	$18^h13^m58\overset{s}{.}10$
Dec.	$-18°54'16\overset{''}{.}7$	$-18°54'16\overset{''}{.}7$	$-18°54'16\overset{''}{.}7$	$-18°54'17\overset{''}{.}0$
Primary beam size (FWHP)	$52''$	$43''$	$34''$	$1\overset{'}{.}9$
Frequency coverage:				Mean continuum: 24.85 GHz
LSB	~216.9–220.9 GHz	~265.7–269.7 GHz	~333.6–337.6 GHz	8 × 8 MHz
USB	~228.9–232.9 GHz	~277.7–281.7 GHz	~345.6–349.6 GHz	8 × 8 MHz
Channel width[a]	0.8125 MHz	0.8125 MHz	0.8125 MHz	31.25 kHz
		0.406 MHz (N_2H^+)		(0.4 km s^{-1})
Resampled velocity resolution	1.12 km s^{-1}	0.92 km s^{-1}	0.75 km s^{-1}	n/a
Gain calibrators	J1733-130, J1924-292	J1733-130, J1924-292	J1733-130, J1924-292	J1820-2528
Bandpass calibrator	3C84	3C279	3C84	J1924-292
Flux calibrator	Callisto[b]	Neptune[b]	Callisto[b]	3C286
Angular resolution[c]	$0\overset{''}{.}574 \times 0\overset{''}{.}370$ (P.A. = 30°)	$0\overset{''}{.}906 \times 0\overset{''}{.}837$ (P.A. = −74°)	$0\overset{''}{.}798 \times 0\overset{''}{.}703$ (P.A. = 54°)	$1\overset{''}{.}077 \times 0\overset{''}{.}833$ (P.A. = −35°)
Largest angular scale[d]	$9''$	$9''$	$9''$	~40$''$
Projected baselines	~20-394 kλ	~17–191 kλ	~18–225 kλ	~1.8–315 kλ
Continuum rms noise[c]	0.7 mJy beam^{-1}	3 mJy beam^{-1}	3 mJy beam^{-1}	75 μJy beam^{-1}
Spectral line rms noise[e]	23 mJy beam^{-1}	71 mJy beam^{-1}	73 mJy beam^{-1}	1.5 mJy beam^{-1}
		150 mJy beam^{-1} (N_2H^+)[f]	55 mJy beam^{-1} (^{12}CO)	

Notes.

[a] 1.1 mm: of 48 correlator "chunks," two have 0.406 MHz and six have 1.625 MHz channels.

[b] Using Butler-JPL-Horizons 2012 models.

[c] Combined LSB+USB continuum image (Briggs weighting, robust = 0.5). VLA NH_3 images were made with robust = 1.0 for best sensitivity.

[d] Scale at which 10% of peak brightness would be recovered for a Gaussian source; for 50% recovery, multiply by 0.55 (Wilner & Welch 1994). VLA: Estimate for combined D+CnB images, which are dominated by the higher-weight CnB data.

[e] Typical rms per channel; Hanning-smoothed.

[f] Near $V_{LSR} \sim 35$ km s^{-1}.

2. OBSERVATIONS

SMA observations of G11.92−0.61 were obtained at 1.3, 1.1, and 0.88 mm, as summarized in Table 1. The data were calibrated and imaged in CASA. For the 2011 data, system temperature calibration was first applied in MIRIAD; for the 2013 data, the sma2casa filler[9] was used. The continuum was estimated in the *uv*-plane, using line-free channels, and subtracted from the line emission. The continuum was then self-calibrated, and the solutions applied to the line data. For each data set, the uniform-spectral-resolution line data (0.8125 MHz channels) were resampled to a common velocity resolution (Table 1), then Hanning-smoothed. (To obtain better spectral resolution on the N_2H^+(3–2) line, a mixed-spectral-resolution mode was employed, see Table 1). The ^{12}CO(3–2) data were further smoothed to 3 km s^{-1}.

The NRAO[10] VLA observations of G11.92−0.61 are part of a survey of massive protostellar objects in 1.3 cm continuum and line emission (Brogan et al. 2011, 2012; C. L. Brogan, in preparation; here we consider only the NH_3 and 1.3 cm continuum data). The VLA data were calibrated, imaged, and self-calibrated in CASA.

Observational parameters and image properties are listed in Table 1. All measurements were made from images corrected for the primary beam response.

3. RESULTS

3.1. Continuum Emission

The continuum emission from the two brightest millimeter cores in the G11.92−0.61 protocluster, MM1 and MM2, is detected with high signal-to-noise ratio in all of our new (sub)millimeter images: observed source properties are summarized in Table 2. Separated from MM2 by only ~7$\overset{''}{.}$2 (0.12 pc), MM1 appears to be a typical hot core (Cyganowski et al. 2011b; Section 3.2), and so provides a useful basis for comparison. For both cores, the ~0$\overset{''}{.}$5 resolution Very Extended configuration (VEX) SMA 1.3 mm image recovers ~40% of the flux density in the ~2$\overset{''}{.}$4 resolution 1.3 mm SMA image and ~80% of the flux density in the ~1$\overset{''}{.}$1 resolution CARMA 1.4 mm image (both from Cyganowski et al. 2011b). The fitted size of MM1 is consistently smaller than the beam (Table 2), indicating that it is unresolved in all three (sub)millimeter images. In contrast, in the highest-resolution SMA image, the fitted size of MM2 is comparable to the beam, and the source appears slightly extended (Figure 1).

To measure (sub)millimeter spectral indices, a 1.3 mm image was made using only those projected baselines spanned by the 1.1 mm data, then convolved to the 1.1 mm synthesized beam.

Table 2
Properties of Continuum Sources

| Source | Observed Properties | | | | | | | | | Derived Properties | | |
| | J2000 Coordinates[a] | | Peak Intensity[a] (mJy beam⁻¹) | Integ. Flux[a] Density (mJy) | Size[a] (″ × ″[P.A.°]) | Size (AU × AU) | T_b (K) | T_{dust} (K) | τ_{dust} | κ_ν[b] (cm² g⁻¹) | M_{gas} ($M_\odot$) | N_{H_2} ×10²⁵ (cm⁻²) | n_{H_2} ×10⁹ (cm⁻³) |
	α (ʰᵐˢ)	δ (°′″)											
SMA 1.3 mm VEX													
MM1	18 13 58.1099	−18 54 20.141	90 (1)	138 (2)	0.34 (0.01) × 0.29 (0.01) [125 (7)]	1150 × 960	34.0	150–240	0.3–0.2	1.11	3–2	0.9–0.5	0.9–0.5
MM2	18 13 57.8599	−18 54 13.958	44 (1)	90 (2)	0.56 (0.02) × 0.36 (0.03) [71 (5)]	1880 × 1220	10.8	16	1.1	1.00	47	6.0	4.0
								17	1.0	1.00	41	5.3	3.5
								19	0.8	1.00	33	4.3	2.8
								20	0.8	1.00	30	3.9	2.6
SMA 1.1 mm EX													
MM1	18 13 58.1102	−18 54 20.201	295 (5)	397 (6)	0.66 (0.02) × 0.36 (0.04) [130 (2)]	2210 × 1200	27.7	150–240	0.2–0.1	1.5	5–3	0.5–0.3	0.3–0.2
MM2	18 13 57.8568	−18 54 13.99	132 (3)	191 (5)	0.61 (0.05) × 0.55 (0.05) [170 (30)]	2100 × 1800	9.4	16	0.9	1.36	48	3.8	1.9
								17	0.8	1.36	43	3.3	1.7
								19	0.7	1.36	35	2.7	1.4
								20	0.6	1.36	32	2.5	1.3
SMA 0.88 mm EX													
MM1	18 13 58.1066	−18 54 20.158	363 (6)	510 (8)	0.58 (0.02) × 0.34 (0.03) [134 (4)]	1940 × 1200	27.1	150–240	0.2–0.1	2.3	3–2	0.3–0.2	0.2–0.1
MM2	18 13 57.8546	−18 54 13.92	167 (5)	294 (9)	0.66 (0.05) × 0.64 (0.05) [4 (46)]	2200 × 2200	7.3	16	0.6	2.11	31	1.9	0.9
								17	0.6	2.11	27	1.7	0.8
								19	0.5	2.11	22	1.4	0.6
								20	0.5	2.11	20	1.3	0.6
VLA 1.3 cm													
CM1	18 13 58.107	−18 54 20.20	0.63(0.08)	⋯	<0.95	<3200							
SMA 1.3 mm VEX: uvrange <191 kλ, convolved to 1.1 mm beam													
MM1	18 13 58.1110	−18 54 20.144	121 (2)	148 (3)									
MM2	18 13 57.8557	−18 54 13.97	71 (2)	103 (3)									
SMA 0.88 mm EX: convolved to 1.1 mm beam													
MM1	18 13 58.1068	−18 54 20.160	388 (6)	525 (8)									
MM2	18 13 57.8532	−18 54 13.91	185 (6)	302 (9)									

Notes.

[a] SMA: from two-dimensional Gaussian fitting; "size" is deconvolved source size. Statistical uncertainties are indicated by the number of significant figures or given in parentheses. VLA: parameters of peak pixel; quoted uncertainties are one pixel (position) and 1σ (peak intensity).

[b] Ossenkopf & Henning (1994): grains with thin (MM1) or thick (MM2) ice mantles and coagulation at 10⁸ cm⁻³; linearly interpolated to 1.1 and 0.88 mm.
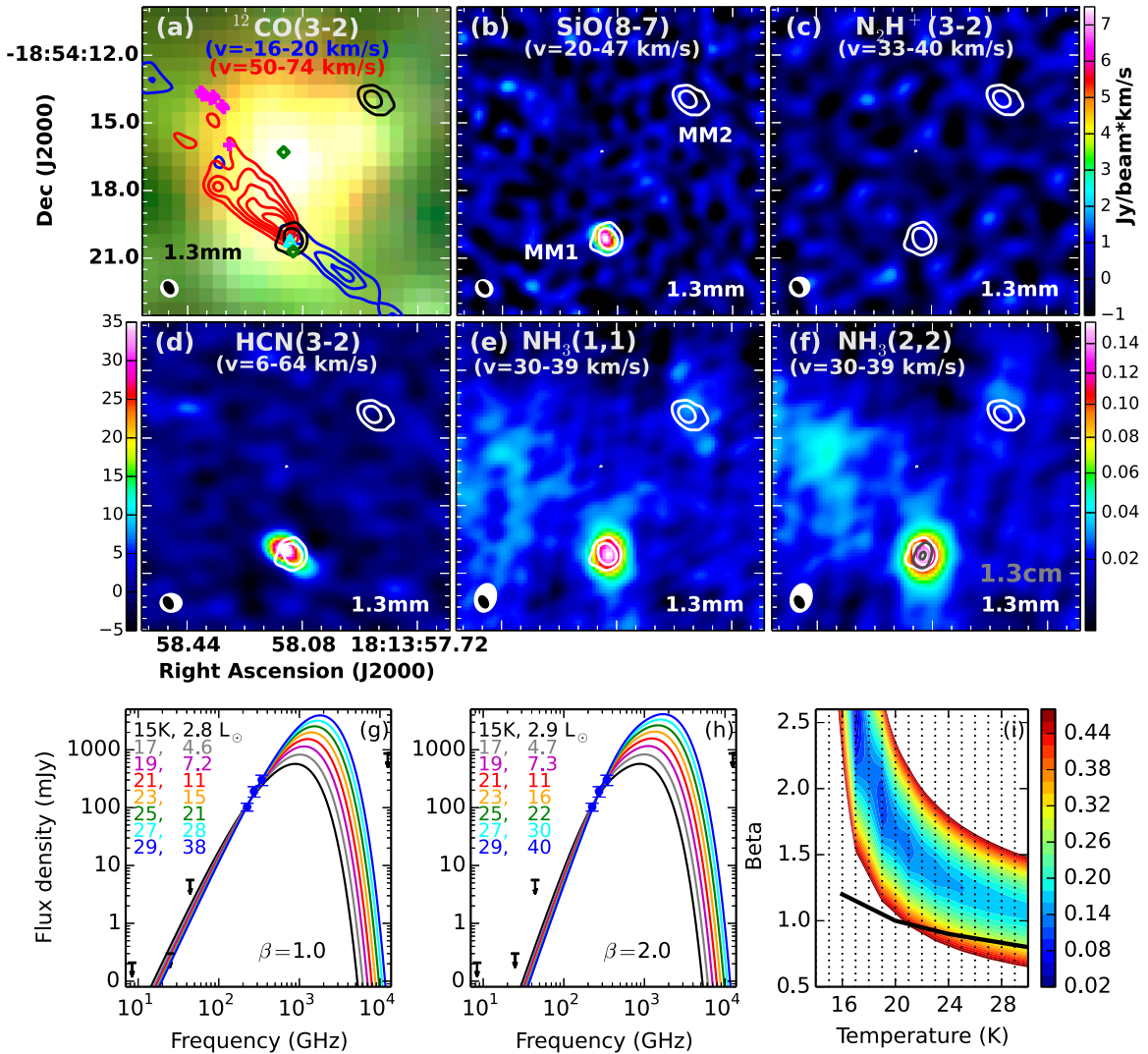
Figure 1. SMA 1.3 mm continuum contours overlaid on (a) three-color *Spitzer* image (RGB: 8.0,4.5,3.6 μm); (b)–(f) integrated intensity maps of selected species. All panels show the same field of view; (b) and (c) and (e) and (f) share color bars. Overlaid are (a) blueshifted/redshifted ^{12}CO(3–2) and masers (Class II ($\diamond$) and Class I (+) CH$_3$OH, Cyganowski et al. 2009; H$_2$O ($\triangle$), Hofner & Churchwell 1996; Breen & Ellingsen 2011) and (f) VLA 1.3 cm continuum contours. (g) and (h) Observed MM2 SED, overplotted with graybody fits from our β-temperature grid (Section 4.2): in the χ^2 surface plot (i), the area below the black line is excluded by our 4σ 1.3 cm limit. Levels: 1.3 mm: $[5, 25] \times \sigma$, $\sigma = 0.7$ mJy beam^{-1}; 1.3 cm: $[5, 8] \times \sigma$, $\sigma = 75\,\mu$Jy beam^{-1}; ^{12}CO: 0.8 Jy beam^{-1} km s^{-1} $\times$ [5, 10, 15] (blue), $\times$[5, 10, 15, 20, 25] (red).

(A color version of this figure is available in the online journal.)

The 0.88 and 1.1 mm observations have roughly comparable *uv*-coverage, so the 0.88 mm image was simply convolved to the 1.1 mm synthesized beam. Flux densities measured from these images are presented in Table 2. In fitting spectral indices, we include the statistical uncertainties (Table 2) and conservative estimates of the absolute flux calibration uncertainty (15% at 1.3 mm, 20% at 1.1 and 0.88 mm). The fitted spectral indices are $\alpha = 3.1 \pm 0.1$ for MM1 and $\alpha = 2.6 \pm 0.1$ for MM2.

Our 1.3 cm VLA continuum image confirms the presence of CM1 (centimeter-wavelength counterpart to MM1; Cyganowski et al. 2011a) at the $\sim 8\sigma$ level (Figure 1, Table 2). Located $\sim 0\farcs07$ (240 AU) southwest of the fitted position of MM1, the (unresolved) 1.3 cm emission is too strong to be due purely to dust ($S_{\rm dust, 1.3\,cm} \sim 0.2$ mJy, assuming $\alpha = 3.1$). No 1.3 cm counterpart to MM2 is detected: the 4σ limit is 0.30 mJy beam^{-1}, corresponding to a limiting size $r \lesssim 17$ AU for any optically thick hypercompact H II region (following Cyganowski et al. 2011a).

3.2. (Lack of) Line Emission

The most remarkable characteristic of MM2 is its lack of (sub)millimeter-wavelength line emission: as shown in Figure 2, the image cubes are devoid of line emission at the MM2 position across ~ 24 GHz of bandwidth observed with the SMA. We searched the spectra at the MM2 continuum peak for $>4\sigma$ excursions in $\geqslant 2$ adjacent channels. The only feature is at $\nu_{\rm observed} = 232.3365$ GHz: an unresolved $\sim 5.5\sigma$ peak coincident with MM2 ($>4\sigma$ in one adjacent channel, $\nu_{\rm observed} = 232.3374$ GHz). Searching the splatalogue line catalog near the expected rest frequency (for $V_{\rm LSR} \sim 35$–37 km s^{-1}) returns primarily transitions with $E_{\rm upper} > 100$ K, inconsistent with the lack of other line emission: the only exception is an unidentified transition, U-232364 ($\nu_{\rm rest} = 232.364$ GHz). Without a plausible identification, the available evidence is insufficient to conclude that this weak, narrow feature represents real line emission associated with MM2. In marked contrast, MM1 exhibits copious line emission in molecules characteristic of hot
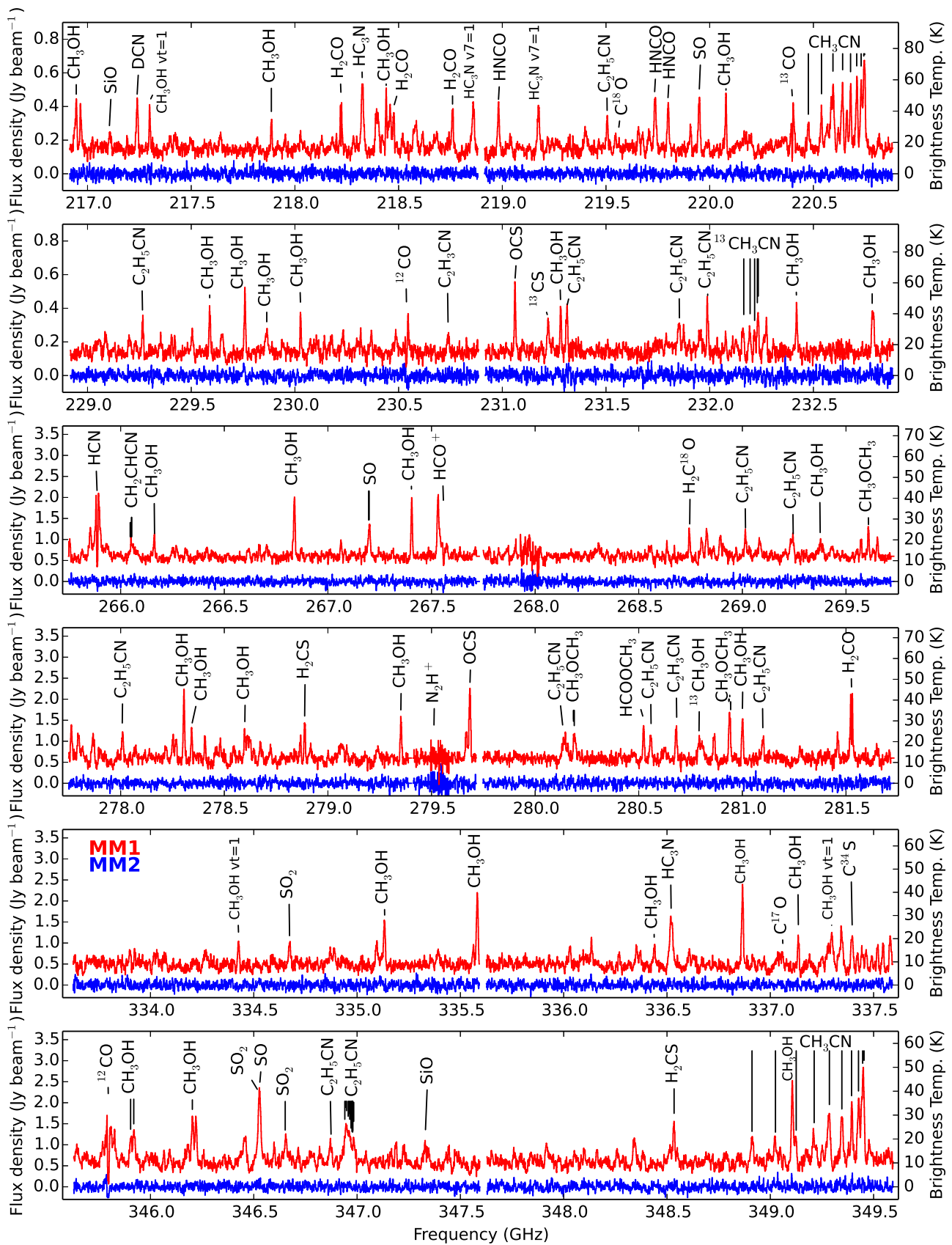
Figure 2. Continuum-subtracted SMA spectra toward the MM1 (red) and MM2 (blue) continuum peaks, showing the full 24 GHz SMA bandwidth. MM1 spectra are offset for clarity. Transition frequencies for selected molecules are labeled for reference.

(A color version of this figure is available in the online journal.)

cores (including CH_3CN, OCS, HC_3N: Figure 2; Cyganowski et al. 2011b).

The SMA spectral setups (and so the nondetections toward MM2) include tracers of cold, dense gas as well as of rich hot-core chemistry. In particular, the 1.1 mm tuning was chosen to cover three diagnostic lines: (1) $N_2H^+(3–2)$ ($E_{upper} \sim 27$ K, $n_{crit} \sim 3 \times 10^6$ cm^{-3}), for a cold (<20 K) core with CO freezeout; (2) $HCO^+(3–2)$ ($E_{upper} \sim 26$ K, $n_{crit} \sim 4 \times 10^6$ cm^{-3}), for a warmer core in which CO has come off the grains; and (3) $HCN(3–2)$ ($E_{upper} \sim 26$ K, $n_{crit} \sim 8 \times 10^7$ cm^{-3}), for a very high-density core. All of these lines are undetected toward MM2, as are (at 1.3 mm) $N_2D^+(3–2)$, a tracer of the inner "deuteration zone" in low-mass starless cores (Caselli et al. 2002; Ceccarelli et al. 2014), $^{12}CO(2–1)$ and its isotopologues (Figures 1 and 2).

Our VLA NH_3 data provide an independent line of evidence, and sensitivity to emission from lower-density gas and on larger spatial scales (Table 1). Like N_2H^+, NH_3 does not deplete onto grains at densities $n_{H_2} \lesssim 10^6$ cm^{-3} (Bergin & Langer 1997); however, n_{crit} for the 1.3 cm NH_3 inversion transitions is >2 orders of magnitude lower than for $N_2H^+(3–2)$. NH_3 emission is detected in the vicinity of MM2, but does not appear to peak on the millimeter core (Figure 1, showing $v = 30–39$ km s^{-1}; see also Section 4.3). In contrast, MM1 is associated with a compact NH_3 core.

In addition to exhibiting much richer chemistry, MM1 differs from MM2 in driving a molecular outflow. As shown in Figure 1, MM1 drives a well-collimated bipolar molecular outflow, traced by high-velocity $^{12}CO(3–2)$ emission. $SiO(8–7)$ and $SiO(5–4)$ are also detected toward MM1, indicative of recently shocked gas, and hence an *active* outflow (Pineau des Forets et al. 1997; Cyganowski et al. 2012). The MM1 outflow was previously imaged, at lower resolution, in $^{12}CO(2–1)$, $HCO^+(1–0)$, and $SiO(2–1)$ by Cyganowski et al. (2011b). The new, higher-resolution data better resolve the outflow lobes, and clearly show that there is no evidence for an outflow driven by MM2.

4. DISCUSSION: THE NATURE OF MM2

4.1. An Extragalactic Interloper?

In the absence of (sub)millimeter line emission, we must consider the chance of MM2 being an extragalactic background source. The Mocanu et al. (2013) catalog, covering 771 deg^2 of the South Pole Telescope Sunyaev–Zel'dovich (SPT-SZ) survey, provides an excellent reference point. The SPT-SZ survey is multi-wavelength ($\lambda = 3.2, 2.0, 1.4$ mm), allowing dusty sources to be distinguished from those dominated by synchrotron emission. The (sub)millimeter-wavelength spectral index and centimeter-wavelength nondetection of MM2 are inconsistent with synchrotron emission, so SPT-SZ dust-dominated sources are the relevant comparison. At 2″4 resolution, the 1.3 mm flux density of MM2 is 0.203 ± 0.014 Jy (Cyganowski et al. 2011b). Considering all dust-dominated SPT-SZ sources, the number density for $S_{1.4 mm} > 0.2$ Jy is ~ 0.002 deg^{-2} (Mocanu et al. 2013, Table 9), corresponding to 4×10^{-7} sources expected within the 1.3 mm SMA primary beam (FWHP). It is thus extremely unlikely that MM2 is a background extragalactic source, and we conclude that MM2 is a member of the G11.92−0.61 (proto)cluster.

4.2. Physical Properties: Estimates from Dust Emission

The combination of physical properties inferred for MM2 from its (sub)millimeter-wavelength continuum emission is extraordinary. We estimate the core gas mass from the observed integrated flux densities using a simple model of isothermal dust emission, correcting for the dust opacity (Cyganowski et al. 2011b, Equation (3)). These estimates, for a range of adopted dust temperatures, are presented in Table 2. Estimates for MM1 are included for comparison: for the hot core, the minimum and maximum adopted temperatures correspond to the two components required to fit the $J = 12–11$ CH_3CN spectrum (using the method of Hunter et al. 2014).

A strict lower limit to the physical temperature of MM2 is provided by its continuum brightness temperature in the 1.3 mm VEX image: 10.8 K. To constrain the dust temperature and opacity index (β), we fit the three (sub)millimeter flux densities (measured from the convolved images, Section 3.1) and their uncertainties with a single-temperature modified graybody for each point in a β-temperature grid ($\beta = 0.5–3.05$, $\Delta\beta = 0.05$; $T = 12–35$ K, $\Delta T = 1$ K). For each β-temperature combination, the only free parameter is $\tau_{1.3 mm}$: the source size is fixed to 0″58, the geometric mean of the fitted size at 1.1 mm. Example graybody fits are shown in Figure 1, along with the χ^2 surface plot for the β-temperature grid. Notably, our 1.3 cm upper limit independently excludes low-β models (Figure 1),[11] suggesting that MM2's moderate (sub)millimeter spectral index ($\alpha = 2.6 \pm 0.1$) is due primarily to high optical depth, as opposed to e.g., large grains (Tobin et al. 2013).

As illustrated in Figure 1(i), the models that best fit MM2 span a fairly narrow temperature range, $\sim 17–19$ K. Adopting $T_{dust} = 20$ K as an approximate upper limit (see also Section 4.3), $M_{gas} \gtrsim 30 M_\odot$ (estimated from the 1.3 mm VEX data; Table 2). Importantly, this mass is condensed into a radius[12] <1000 AU. Assuming spherical symmetry, this implies $N_{H_2} > 10^{25}$ cm^{-2} and $n_{H_2} > 10^9$ cm^{-3}. The luminosity estimate from the spectral energy distribution (SED) yields $L/M \sim 0.1–0.3$ ($T = 17–20$ K), indicative of the earliest phases in models of massive young stellar object evolution (Molinari et al. 2008).

4.3. Astrochemical Modeling

The dearth of line emission toward MM2 suggests extreme depletion of gas-species due to freeze-out onto grains, as seen in cold, dense low-mass prestellar cores ($n_{H,max} \sim 10^8$ cm^{-3}; Caselli 2011; Ceccarelli et al. 2014). To explore the possible physical properties consistent with the lack of molecular emission lines, we ran a grid of gas-grain astrochemical models using MONACO (Vasyunin et al. 2009) and the Ohio State University gas-grain reaction network (Garrod et al. 2008). We used MONACO to model the time evolution of gas-phase and grain surface chemistry under a fixed set of physical conditions. All models were run with oxygen-rich, low-metal elemental abundances (Graedel et al. 1982), a standard dust-to-gas mass ratio and surface site density (0.01 and 1.5×10^{15} sites cm^{-2}, respectively; Semenov et al. 2003), a 10% reactive desorption efficiency (Vasyunin & Herbst 2013) and a standard molecular cloud cosmic ray ionization (CRI) rate ($\zeta_{CRI} = 1.3 \times 10^{-17}$ s^{-1}, attenuated from the diffuse interstellar medium; Vasyunin et al. 2009; Padovani et al. 2009). The standard ζ_{CRI} is probably too high for this source, since at the very high column densities inferred from the dust emission additional CR attenuation is expected, as discussed below. The model grid comprises

---

[11] Upper limits are plotted, but not used in the graybody fits: 4σ VLA limits at 0.7, 3.6, and 1.3 cm (Cyganowski et al. 2009, 2011a, this work), MIPSGAL 24 μm limit (maximum flux density of a point source that would produce the observed intensity of the pixel coincident with MM2).

[12] $r \equiv 1/2\sqrt{\theta_{min}\theta_{maj}}$
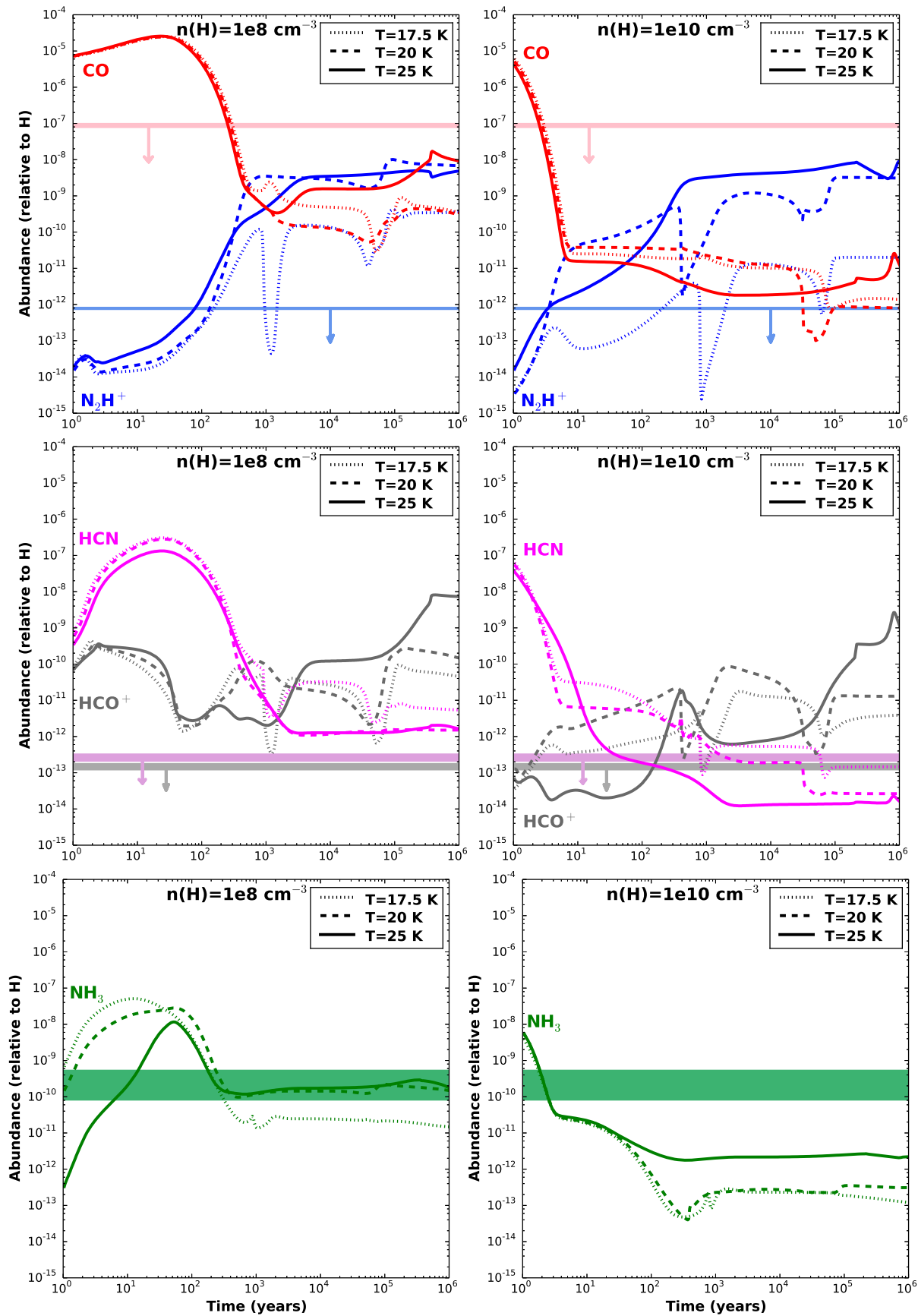
Figure 3. Time-dependent molecular abundances from gas-grain chemical models ($A_V = 100$); horizontal bands show observed abundances and upper limits (with arrows). Model predictions and observations should only be compared at $t \gtrsim 10^3$ years, since the meaning of model predictions at shorter times is unclear. Observed N_2H^+ and HCN limits are only reproduced at low temperatures and high densities, respectively.

(A color version of this figure is available in the online journal.)

seven temperatures (10–25 K, $\Delta T = 2.5$ K), five densities[13] (1 $\times$ 10^8–1 $\times$ 10^{10} cm^{-3}), and four A_V (10, 100, 1000, 10000). Increasing A_V above 100 has no effect; Figure 3 presents results for $A_V = 100$.

To quantitatively compare MM2's chemistry with the gas-grain models, we estimate molecular abundance limits from the SMA data for four potentially diagnostic species within our observing bands.[14] Using RADEX (van der Tak et al. 2007), we find the molecular column density equivalent to our 4σ T_B limit for an assumed linewidth of 2 km s^{-1} and a suite of temperatures (15–25 K, $\Delta T = 2.5$ K) informed by the SED modeling. For N$_2$H$^+$, this yields column density limits only for $T \geqslant 20$ K; if $T < 20$ K the SMA surface brightness sensitivity is insufficient to detect even optically thick emission.[15] Molecular abundances, χ(MOL) $= N$(MOL)$/N$(H), are calculated adopting N(H) $= 2 \times N$(H$_2$), with N(H$_2$) calculated from the (sub)millimeter continuum emission in the same SMA data set as the line of interest (e.g., 1.1 mm for N$_2$H$^+$) for each (assumed) temperature. Figure 3 presents the resulting limits as horizontal stripes: vertical extent reflects the range in assumed temperature. We emphasize that there are substantial inherent uncertainties (e.g., linewidth, temperature, estimation of N(H$_2$)), and the derived abundance limits should be considered order-of-magnitude estimates. For NH$_3$, additional uncertainty is introduced by the difference in morphology between the NH$_3$ and dust continuum emission (Figure 1) and the difference in uv-coverage between the VLA and SMA data. We use the VLA spectra at the MM2 continuum peak to estimate N(NH$_3$) (following Cyganowski et al. 2013), and calculate χ(NH$_3$) for $T_{dust} = 15$–25 K using two different measures of N(H$_2$): our 1.1 mm SMA data and the 1.3 mm compact-configuration SMA data from Cyganowski et al. (2011b). Figure 3 shows the resulting χ(NH$_3$) range (green rectangles).

Comparing the data and models after the initial freezeout (Figure 3; $t \gtrsim 10^3$ years) shows that it is possible to explain the observed dearth of molecular emission assuming a standard gas-grain chemistry if the MM2 conditions are indeed as extreme as suggested by the SED modeling. Furthermore, specific model predictions provide three key insights. (1) The non-detection of N$_2$H$^+$ rules out $T \geqslant 20$ K for MM2. For $T \geqslant 20$ K, the model-predicted N$_2$H$^+$ abundances exceed the observational limit by $\gtrsim 3$ orders of magnitude. (2) The non-detection of HCN favors the highest density models. For $T < 20$ K and n(H)$\sim 10^{10}$ cm^{-3}, the model-predicted HCN abundances are consistent with the observational limit, within the observational uncertainties and $\sim$order-of-magnitude uncertainty intrinsic in the model results (Vasyunin et al. 2004, 2008). Lower-density models ($\sim 10^8$ cm^{-3}) predict higher χ(HCN), above the observed limit for all times and temperatures. (3) The NH$_3$ detected with the VLA near MM2 cannot trace the dense gas seen in dust continuum emission with the SMA. The inferred NH$_3$ abundance is $\sim 10^3$ times higher than predicted by the cold, dense models required by the SMA nondetections of N$_2$H$^+$ and HCN; instead, χ(NH$_3$) is consistent with comparatively lower-density ($\sim 10^8$ cm^{-3}), warmer (20–25 K) material. From simple estimates, external heating by MM1/MM3 ($L \sim 10^4$ $L_\odot$, Cyganowski et al. 2011b) is sufficient to account for NH$_3$ temperatures of $\sim$20 K near MM2.

The poor model-data agreement for HCO$^+$ even at high densities suggests that ζ_{CRI} is too high (the agreement is worse for lower-density models): a lower CRI rate (e.g., attenuated within the high-density core; Padovani et al. 2013, Figure 1) would reduce the model-predicted abundances. Overestimated desorption rates could, however, also overpredict χ(HCO$^+$). Evaluating the level of CR attenuation would require new, deep observations of the only observable ions expected not to freeze out under any temperature and density conditions: H$_2$D$^+$ and D$_2$H$^+$ (e.g., Ceccarelli & Dominik 2005).

4.4. The Best Candidate?

Based on the available evidence, MM2 is the best candidate for a massive starless core discovered to date. Crucially, MM2 has a centrally condensed mass sufficient to form a massive star: $\gtrsim 30$ $M_\odot$ within R < 1000 AU. Compared to CygX-N53-MM2 (another contender for "best candidate"), G11.92−0.61−MM2 has $\gtrsim 5\times$ as much mass on $\sim$1500 AU sizescales (estimated from millimeter continuum emission; Bontemps et al. 2010). Duarte-Cabral et al. (2013) also report a tentative outflow detection toward CygX-N53-MM2, raising the question of whether it is truly starless. Compared to the Tan et al. (2013) cores, G11.92−0.61−MM2 is more massive (with the possible exception of C1-S), more compact, and several orders of magnitude denser. G11.92−0.61−MM2 has also been more extensively and sensitively searched for star formation indicators.

Interestingly, Kauffmann et al. (2013) recently proposed that very short lifetimes could explain the lack of observational examples of massive starless cores, consistent with the very short free-fall time ($\lesssim 1000$ yr) implied by MM2's high density. Further comparison of MM2's properties with the predictions of core accretion models for massive star formation requires additional observations, e.g., of the dense-core tracers H$_2$D$^+$, N$_2$H$^+$, and N$_2$D$^+$ with the sensitivity of ALMA. Most important is detecting line emission from the dense, cold millimeter core to determine whether MM2 is gravitationally bound and will collapse to form a massive star.

REFERENCES

Alves, J., Lombardi, M., & Lada, C. J. 2007, A&A, 462, L17
Bergin, E. A., & Langer, W. D. 1997, ApJ, 486, 316
Bonnell, I. A., & Smith, R. J. 2011, in IAU Symp. 270, Computational Star Formation, ed. J. Alves, B. Elmegreen, J. M. Girart, & V. Trimble (Cambridge: Cambridge Univ. Press), 57
Bontemps, S., Motte, F., Csengeri, T., & Schneider, N. 2010, A&A, 524, A18
Breen, S. L., & Ellingsen, S. P. 2011, MNRAS, 416, 178
Brogan, C. L., Hunter, T. R., Cyganowski, C. J., et al. 2011, ApJL, 739, L16
Brogan, C. L., Hunter, T. R., Cyganowski, C. J., et al. 2012, in IAU Symp. 287, Cosmic Masers—from OH to Ho, ed. R. S. Booth, E. M. L. Humphreys, & W. H. T. Vlemmings (Cambridge: Cambridge Univ. Press), 497
Caselli, P. 2011, in IAU Symp. 280, The Molecular Universe, ed. J. Cernicharo & R. Bachiller (Cambridge: Cambridge Univ. Press), 19
Caselli, P., Benson, P. J., Myers, P. C., & Tafalla, M. 2002, ApJ, 572, 238
Ceccarelli, C., Caselli, P., Bockelee-Morvan, D., et al. 2014, arXiv:1403.7143
Ceccarelli, C., & Dominik, C. 2005, in Proc. of the Dusty and Molecular Universe. A Prelude to Herschel and ALMA, ed. A. Wilson (ESA SP-577, Noordwijk: ESA), 349
Cyganowski, C. J., Brogan, C. L., Hunter, T. R., & Churchwell, E. 2009, ApJ, 702, 1615
Cyganowski, C. J., Brogan, C. L., Hunter, T. R., & Churchwell, E. 2011a, ApJ, 743, 56

---

[13] n(H)$_{total} = n$(H) $+ 2 \times n$(H$_2$).

[14] χ(CO) is estimated from C^{18}O(2–1) assuming N(CO)$/N$(C^{18}O) $= 336$ (Wilson & Rood 1994).

[15] N$_2$H$^+$ is undetected toward MM1, as expected for a hot core: once CO desorbs, the N$_2$H$^+$+CO→HCO$^+$+N$_2$ destruction channel becomes active.

Cyganowski, C. J., Brogan, C. L., Hunter, T. R., Churchwell, E., & Zhang, Q. 2011b, ApJ, 729, 124
Cyganowski, C. J., Brogan, C. L., Hunter, T. R., et al. 2012, ApJL, 760, L20
Cyganowski, C. J., Koda, J., Rosolowsky, E., et al. 2013, ApJ, 764, 61
Cyganowski, C. J., Whitney, B. A., Holden, E., et al. 2008, AJ, 136, 2391
Duarte-Cabral, A., Bontemps, S., Motte, F., et al. 2013, A&A, 558, A125
Garrod, R. T., Weaver, S. L. W., & Herbst, E. 2008, ApJ, 682, 283
Graedel, T. E., Langer, W. D., & Frerking, M. A. 1982, ApJS, 48, 321
Hofner, P., & Churchwell, E. 1996, A&AS, 120, 283
Hunter, T. R., Brogan, C. L., Cyganowski, C. J., & Young, K. H. 2014, ApJ, 788, 187
Kauffmann, J., Pillai, T., & Goldsmith, P. F. 2013, ApJ, 779, 185
McKee, C. F., & Tan, J. C. 2002, Natur, 416, 59
McKee, C. F., & Tan, J. C. 2003, ApJ, 585, 850
Mocanu, L. M., Crawford, T. M., Vieira, J. D., et al. 2013, ApJ, 779, 61
Molinari, S., Pezzuto, S., Cesaroni, R., et al. 2008, A&A, 481, 345
Myers, A. T., McKee, C. F., Cunningham, A. J., Klein, R. I., & Krumholz, M. R. 2013, ApJ, 766, 97
Ossenkopf, V., & Henning, T. 1994, A&A, 291, 943
Padovani, M., Galli, D., & Glassgold, A. E. 2009, A&A, 501, 619
Padovani, M., Hennebelle, P., & Galli, D. 2013, A&A, 560, A114

Pineau des Forets, G., Flower, D. R., & Chieze, J.-P. 1997, in IAU Symp. 182, Herbig-Haro Flows and the Birth of Stars, ed. B. Reipurth & C. Bertout (Dordrecht: Kluwer), 199
Rathborne, J. M., Lada, C. J., Muench, A. A., et al. 2009, ApJ, 699, 742
Sato, M., Wu, Y. W., Immer, K., et al. 2014, ApJ, 793, 72
Semenov, D., Henning, T., Helling, C., Ilgner, M., & Sedlmayr, E. 2003, A&A, 410, 611
Smith, R. J., Longmore, S., & Bonnell, I. 2009, MNRAS, 400, 1775
Tan, J. C., Beltran, M. T., Caselli, P., et al. 2014, arXiv:1402.0919
Tan, J. C., Kong, S., Butler, M. J., Caselli, P., & Fontani, F. 2013, ApJ, 779, 96
Tobin, J. J., Hartmann, L., Chiang, H.-F., et al. 2013, ApJ, 771, 48
van der Tak, F. F. S., Black, J. H., Schöier, F. L., Jansen, D. J., & van Dishoeck, E. F. 2007, A&A, 468, 627
Vasyunin, A. I., & Herbst, E. 2013, ApJ, 769, 34
Vasyunin, A. I., Semenov, D., Henning, T., et al. 2008, ApJ, 672, 629
Vasyunin, A. I., Semenov, D. A., Wiebe, D. S., & Henning, T. 2009, ApJ, 691, 1459
Vasyunin, A. I., Sobolev, A. M., Wiebe, D. S., & Semenov, D. A. 2004, AstL, 30, 566
Wilner, D. J., & Welch, W. J. 1994, ApJ, 427, 898
Wilson, T. L., & Rood, R. 1994, ARA&A, 32, 191